minerals

MDPI

Article

Exploring the High-Pressure Phases of Carbon through X-ray Diffraction of Dynamic Compression Experiments on Sandia's Z Pulsed Power Facility

Tommy Ao [1,*], Pat Kalita [1], Caroline Blada [1], Nathan P. Brown [1], Karin Fulford [1], Paul Gard [1], Matthias Geissel [1], Heath Hanshaw [1], Michael Montoya [1], Sheri Payne [2], Edward Scoglietti [1], Anthony Smith [1], Christopher Shane Speas [1], John L. Porter [1] and Christopher T. Seagle [1]

[1] Sandia National Laboratories, Albuquerque, NM 87185, USA; hlhansh@sandia.gov (H.H.); mmmonto@sandia.gov (M.M.); escogli@sandia.gov (E.S.); smith572@llnl.gov (A.S.); csspeas@sandia.gov (C.S.S.); jlporte@sandia.gov (J.L.P.); ctseagl@sandia.gov (C.T.S.)
[2] Mission Support and Test Services, LLC, Albuquerque, NM 87185, USA; slpayne@sandia.gov
* Correspondence: tao@sandia.gov

Abstract: The carbon phase diagram is rich with polymorphs which possess very different physical and optical properties ideal for different scientific and engineering applications. An understanding of the dynamically driven phase transitions in carbon is particularly important for applications in inertial confinement fusion, as well as planetary and meteorite impact histories. Experiments on the Z Pulsed Power Facility at Sandia National Laboratories generate dynamically compressed high-pressure states of matter with exceptional uniformity, duration, and size that are ideal for investigations of fundamental material properties. X-ray diffraction (XRD) is an important material physics measurement because it enables direct observation of the strain and compression of the crystal lattice, and it enables the detection and identification of phase transitions. Several unique challenges of dynamic compression experiments on Z prevent using XRD systems typically utilized at other dynamic compression facilities, so novel XRD diagnostics have been designed and implemented. We performed experiments on Z to shock compress carbon (pyrolytic graphite) samples to pressures of 150–320 GPa. The Z-Beamlet Laser generated Mn-He$_\alpha$ (6.2 keV) X-rays to probe the shock-compressed carbon sample, and the new XRD diagnostics measured changes in the diffraction pattern as the carbon transformed into its high-pressure phases. Quantitative analysis of the dynamic XRD patterns in combination with continuum velocimetry information constrained the stability fields and melting of high-pressure carbon polymorphs.

Keywords: dynamic compression; pulsed power; X-ray diffraction; high-pressure; phase change; carbon

Citation: Ao, T.; Kalita, P.; Blada, C.; Brown, N.P.; Fulford, K.; Gard, P.; Geissel, M.; Hanshaw, H.; Montoya, M.; Payne, S.; et al. Exploring the High-Pressure Phases of Carbon through X-ray Diffraction of Dynamic Compression Experiments on Sandia's Z Pulsed Power Facility. *Minerals* **2023**, *13*, 1203. https://doi.org/10.3390/min13091203

Academic Editor: Daniel Hummer

Received: 11 July 2023
Revised: 1 September 2023
Accepted: 8 September 2023
Published: 13 September 2023

1. Introduction

Carbon is an abundant element that has fundamental importance in many scientific fields and applications. Because of its chemical flexibility, carbon is the basis of numerous organic molecules which can create large molecular compounds that make up living organisms. Carbon fibers have been used to strengthen materials in various industries such as automotive, aerospace, military, and recreational applications.

The high-pressure and high-temperature phase diagram and equation of state (EOS) of carbon [1–3] have recently received strong interest due to their relevance to planetary and stellar physics [4] and inertial confinement fusion (ICF) research [5]. A comprehensive understanding of carbon under extreme conditions is needed to develop better models for our outer planets, extrasolar carbon planets [6], and white dwarf stars [7,8]. For example, Neptune and Uranus are thought to contain large amounts of carbon, mostly as methane, that, under the high pressure and temperature within their ice layers, exists

as diamond [9–11]. Also, the use of high-density carbon for implosion capsule ablators played a significant role in the recent breakthrough ICF experiments that finally achieved controlled nuclear fusion ignition in the laboratory [12–14].

At ambient conditions, elemental carbon generally exists as graphite, which is comprised of stacked hexagonal layers of carbon atoms. The most common form of graphite has an ABAB stacking of the hexagonal layers and is known as hexagonal graphite (HG) [15]. Alternatively, rhombohedral graphite (RG) has an ABCABC stacking and has been found in small quantities within HG materials. Bulk carbon specimens created through thermal decomposition (pyrolysis) of a hydrocarbon gas onto a heated substrate are known as pyrolytic graphite (PG) [16]. Because of the fairly random deposition process, the stacking of the hexagonal layers is sufficiently disordered, and parallel adjacent layers are oriented arbitrarily with respect to one another. As-deposited PG consists of small crystallites that range from tens to hundreds of nm in size [17], and it typically has a density of 2.2 g/cm^3. The compressive annealing of PG allows the crystallites to become better aligned to the HG crystal structure and increases the average crystallite size to ~1 mm, which produces what is known as highly oriented pyrolytic graphite (HOPG) [18].

Above several to tens of gigapascals, cubic diamond (CD) (density of 3.5 g/cm^3) is the stable phase of carbon [19], which comprises the majority of all natural and synthetic diamonds [20]. The CD structure is the face-centered cubic Bravais lattice with a two-atomic basis, in which one carbon atom is on the lattice point, and the other carbon atom is shifted by $\frac{1}{4}$ along each axis. This forms a tetrahedral structure where each carbon atom is covalently bonded to four equal-distanced neighbors. Because of its exceptional strength and hardness, high thermal conductivity, unique optical properties and chemical inertness, CD has been an important material for various technical and industrial applications [21,22]. Thus, the synthesis of diamonds through the heat and compression of graphite has been the subject of intense research for many decades [23].

Hexagonal diamond (HD) is a polymorph of diamond that has a hexagonal unit cell, which was discovered naturally and first synthesized in the laboratory in the 1960s. In nature, HD was first identified based on X-ray diffraction measurements of fragments from the Canyon Diablo meteorite by Hanneman et al. [24]. It was proposed that upon impact with Earth, the intense shock pressure transformed the pre-impact graphite portions within the meteorite into small HD clusters, forming a mineral designated as 'lonsdaleite' [25]. Bundy and Kasper reported the first synthesis of HD in the laboratory under a static pressure exceeding 13 GPa and a temperature greater than 1000 °C [26]. Although HD potentially has superior mechanical properties (e.g., compressive strength, hardness, and rigidity) compared to CD, these advantages have been difficult to verify due to the inability to synthesize HD as a pure phase. Consequently, the actual existence of HD has been questioned, and recent studies have suggested that the previous discoveries of HD may be explained as faulted and twinned CD [27,28].

Static compression experiments have been utilized extensively to synthesize and examine the graphite-to-diamond transformation [22,26,29–31]. The overall findings revealed that HG, RG, PG, and amorphous carbon transformed to CD, but only highly ordered HG could transform to HD [26,31]. Dynamic compression experiments provide alternative thermodynamic loading paths for phase transformations. In addition, the extremely short time scale (nanoseconds) of shock compression experiments is more analogous to the rapid formation of HD within meteorite impacts. In 1961, DeCarli and Jamieson [32] first reported the recovery of CD after the explosive-driven shock compression of graphite. However, it was not until the early 1990s that velocimetry wave-profile analysis of gas-gun plate impact experiments by Erskine and Nellis [33,34] provided real-time evidence of the graphite-to-diamond transformation. Although these continuum measurements indicated the occurrence of the phase change, they did not provide the crystal structure of the new high-pressure phase. Later, the advent of in situ X-ray diffraction (XRD) measurements on dynamic compression platforms [35–38] enabled direct observations of the crystal structure of shock-compressed materials on nanosecond timescales.

Recently, there have been considerable efforts to explore the high-pressure phases of carbon using assorted dynamic compression platforms, such as gas-guns [39–41], high-powered lasers [42–45], and pulsed power generators [46]. For example, Kraus et al. [45] performed laser-driven shock-compression experiments on PG and porous graphite samples and measured in situ XRD using the X-ray free electron laser (XFEL) at the Linac Coherent Light Source (LCLS). It was reported that both PG and porous graphite samples transformed to CD above 50 GPa, and the porous graphite sample melted to liquid carbon at 100 GPa. Interestingly, at higher pressures of 170–228 GPa, the PG sample was claimed to have transformed into HD based on the observation of two closely spaced peaks within a small XRD angular range that were indexed to the HD structure. However, Murri et al. [47] questioned that interpretation and suggested the two peaks may be of coexisting CD structures originating from different strain regions within the shocked sample. Along with the dynamic experiments, various molecular dynamics (MD) simulations have been performed to study the kinetics of the phase transformation of graphite to diamond [48–51].

Alternatively, Turneaure et al. [39] performed gas-gun plate impact experiments on HOPG samples and measured in situ XRD using the synchrotron X-rays at the Dynamic Compression Sector (DCS) of the Advanced Photon Source (APS). The plate impact technique enabled a well-defined shock pressure state to be produced, and a wide XRD angular range detector was used to constrain the indexing of XRD peaks. It was determined that a HOPG sample shock-compressed along the c-axis to 50 GPa transformed into highly oriented elastically strained HD. Volz et al. [40] performed subsequent in situ XRD gas-gun impact plate experiments on HOPG and as-deposited PG samples. The HOPG sample also transformed to HD at 50 GPa, while the PG sample transformed to CD at 60 GPa, thus establishing the role of an initial meso-crystal structure in the graphite-to-diamond transformation.

However, the discrepancy between the laser-driven and gas-gun plate impact experiments remains unresolved. Specifically, the phase transformation of the PG samples to HD after shock-compression to pressures of 170–228 GPa as reported by the laser-driven results (at LCLS-XFEL) could not be corroborated by gas-gun plate impact experiments (at APS-DCS) due to their lower pressure range. In order to achieve these higher pressures, pulsed power-driven plate impact experiments are needed. Recently, in situ XRD diagnostics have been implemented on Sandia's Z Pulsed Power Facility that enable the diagnosis of the crystallographic structure and lattice parameters of shock- and ramp-compressed samples while withstanding the harsh Z environment. In this paper, we present the results of experiments performed on Z that shock-compressed carbon PG samples to pressures of 150–320 GPa and the measured high-pressure phases of carbon using the new Z-XRD diagnostics.

2. Materials and Methods

2.1. Dynamic Compression Concepts

Dynamic compression techniques have been used extensively to collect information on the high-pressure EOS of materials [52–55]. In [56], Forbes presents a thorough review of the scientific field of shock waves phenomena that incorporates information from several disciplines of physics, including hydrodynamics, thermodynamics, electrodynamics, continuum mechanics, and quantum mechanics. In most cases, one-dimensional (1D) plane shock waves in a continuum fluid may be assumed, which enables the basic physics and hydrodynamics to be explained simply. The Hugoniot curve of a material is the locus of states that can be reached by compressing it from its initial state using shocks of various amplitudes. The high-pressure response of a material is determined through the use of the Rankine–Hugoniot jump conditions that connect compressed and undisturbed states [57], which are derived from the conservation of mass:

$$\frac{\rho_0}{\rho} = 1 - \frac{u}{U}; \tag{1}$$

conservation of momentum:

$$P - P_0 = \rho_0 U u; \tag{2}$$

and conservation of energy:

$$E - E_0 = \frac{1}{2}(P + P_0)\left(\frac{1}{\rho_0} - \frac{1}{\rho}\right). \quad (3)$$

For a shock propagating through a material with the shock velocity U, the material within the shock has the particle velocity u. Equations (1)–(3) give the mass density, pressure, and internal energy (ρ, P, and E) within the shock, and the subscript 0 denotes the initial state. It has been shown experimentally that many materials exhibit the following relationship between shock velocity and particle velocity:

$$U = C + Su + Tu^2 \quad (4)$$

where C, S, and T are fitting parameters. Over a large range of velocities, the relationship is linear, and the small quadratic correction in Equation (4) may be ignored.

The impedance-match method is a well-established technique for determining the high-pressure states of materials under dynamic compression, and detailed explanations are given in [58–60]. Overall, the resulting shock states may be understood visually by examining P-u graphs, such as those shown in Figure 1. The shock impedance of a material is defined as ρU, and the higher its shock impedance is, the steeper its Hugoniot curve is. For example, Figure 1a describes the shock loading of a sample B by an impactor A with an impact velocity of u_I. Upon impact, a shock wave propagates to the right in sample, while a shock wave propagates to the left in the impactor. At the impactor-sample interface, the pressure and particle velocity must be conserved so the Hugoniot curves of impactor and sample are connected at P_H and u_H. Figure 1b describes the shock prorogation from a sample B into a window C, in which the window has a lower impedance than the sample. At the sample-window interface, the pressure and particle velocity are conserved and connected at P_L and u_L, but the shock state's pressure is lowered.

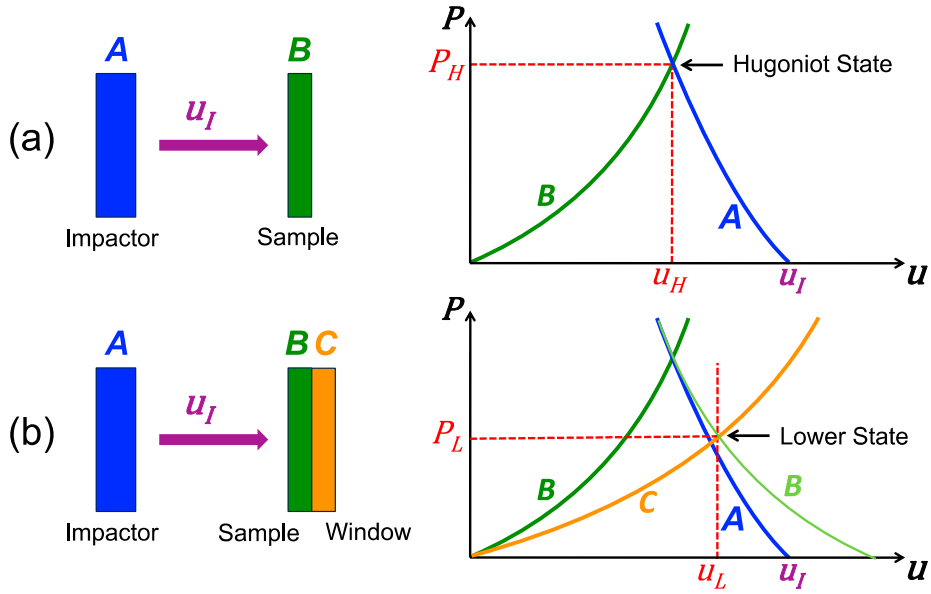

Figure 1. Impedance-matching of (**a**) the shock loading from an impactor A onto a sample B, and (**b**) the shock propagation from a sample B into a window C.

2.2. Pulsed Power Dynamic Compression

The Z Pulsed Power Facility at Sandia National Laboratories is a large, pulsed power facility (~30 m in diameter) that has 22 MJ of stored electrical energy in its Marx generators' capacitors, which can produce a shaped electrical pulse with highly controllable rise time (100–1200 ns) and peak current up to 26 MA [61,62]. Pulse shaping is accomplished by a series of switches and low-inductance transmission lines that compress the electrical

energy in time and direct it into the experimental load at the center of Z. Using the so-called Dynamic Material Property (DMP) configuration, Z dynamically compresses matter to extreme states (with outstanding uniformity, duration, and size) for the investigations of fundamental material properties at high-energy-density (HED) conditions.

Various shock compression experiments on Z have investigated the response of materials along their principal Hugoniots. Figure 2 shows the Z-DMP experimental load designed for the shock compression of multiple samples. The large currents of Z are directed into the parallel plates load consisting of two anode plates arranged around a central cathode stalk to form two anode–cathode (A–K) vacuum gaps. Through a shorting cap at the top of the load, a short circuit is created between the anode plates and the cathode stalk. The current density **J** flowing on the anode and cathode generates a planar magnetic field **B** between them. The resulting $\mathbf{J} \times \mathbf{B}$ force produces a smooth mechanical stress wave that is proportional to the magnetic field squared, which provides sufficient momentum to launch the anode flyer plates at high velocities across the vacuum gaps toward the samples located on the load assemblies (e.g., north and south). Because the Z-DMP load is fairly large (e.g., 56 mm tall, 35 mm wide, and 20 mm thick), the numerous bulk samples (5–10 mm in diameter and 0.5–1 mm in thickness) placed vertically along each of the north and south assemblies experience nearly identical impact conditions.

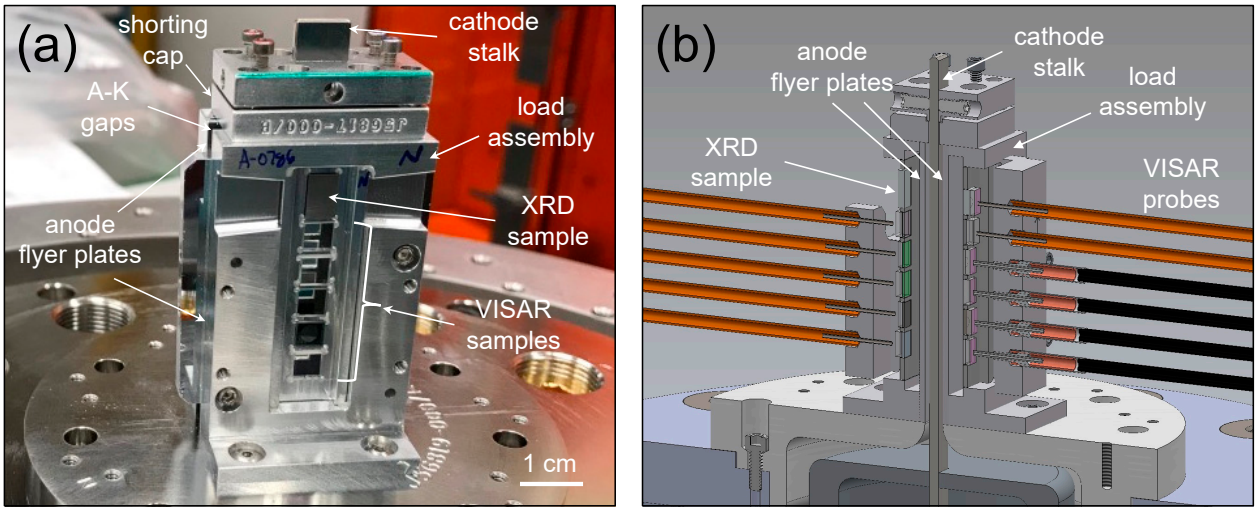

Figure 2. Z-DMP experimental load: (**a**) photo showing the multiple samples for the VISAR measurements and the single sample for the XRD measurement, and (**b**) cross-section view showing the cathode stalk and the anode flyer plates where the large currents and magnetic fields exist.

Velocimetry diagnostics such as Velocity Interferometer System for Any Reflector (VISAR) [63] are typically used to track the particle velocity profiles of the sample. The VISAR diagnostic operates by illuminating coherent light onto a moving surface, and the reflected light is sent into an interferometer. The output signal from the interferometer contains the input signal and a time-delayed version of the input signal and is recorded by a fast optical detector where the measured fringe shift corresponds to the moving surface's velocity. Since the magnetically launched anode flyer plates are able to achieve velocities > 30 km/s, the shock-compressed samples may reach pressures up to tens of Mbar.

Z has several distinctive experimental challenges that prevent utilizing the XRD systems that have functioned at other HED facilities, such as the National Ignition Facility (NIF) at Lawrence Livermore National Laboratory [36], the OMEGA Laser Facility at the University of Rochester [35], the LCLS at SLAC National Accelerator Laboratory [37], and the APS-DCS at Argonne National Laboratory [38]. First, the Z samples are thick (e.g., 0.5–1 mm), and the surrounding hardware consists of high-Z materials that attenuate X-ray transmission, so a reflection geometry is more advantageous for Z-XRD. Second, Z's large

currents and magnetic fields generate a great amount of high-energy photons, including MeV-scale photons near the load, that result in a very high X-ray background. Third, a massive electromagnetic pulse is released when Z discharges that could damage electronics within the load region or prematurely trigger diagnostics. Lastly, the environment of Z is very destructive. During an experiment, 2 MJ of electrical energy is released into the central load region of Z, which causes the Z-DMP load to explode, generating 10′s–100′s km/s debris field. To overcome these challenges, two novel schemes for in situ XRD on Z were developed: (1) a 'time-integrated' system called the Spherical Crystal Diffraction Imager (SCDI) diagnostic, and (2) a 'time-gated' system called the DIffraction SCintillator Optic (DISCO) diagnostic.

2.3. Z-XRD Diagnostics

X-ray diffraction of a crystalline solid is the coherent scattering of X-rays from its crystal lattice in which the X-ray's wavelength and the crystal's d-spacing satisfy Bragg's law. A polycrystalline sample comprises of a large number of randomly oriented discrete crystals, so many of them will have the correct orientation that satisfy Bragg's law. After a polycrystalline sample is illuminated by a monochromatic X-ray beam, the X-rays are diffracted into scattering patterns called Debye–Scherrer cones. When a two-dimensional (2D) X-ray detector is fielded such that it intersects a plane of multiple diffraction cones, a polycrystalline or powder XRD pattern may be acquired. However, any X-ray detector placed near the Z-DMP load that stores the data locally would be destroyed by the debris field before the XRD pattern could be recovered.

2.3.1. Spherical Crystal Diffraction Imager (SCDI)

In the Spherical Crystal Diffraction Imager (SCDI) scheme, a spherically bent crystal is fielded instead of a 2D X-ray detector to intersect the Debye–Scherrer cones and to relay-image the XRD pattern into a well-protected sensor. Fundamentally, the SCDI diagnostic is a bent-crystal microscope that operates within a narrow spectral bandwidth to measure nearly monochromatic images and enables high spatial resolution over a cm-sized field of view. Its design is analogous to the spherical crystal X-ray backlighter diagnostic routinely fielded on ICF experiments on Z [64–66].

Figure 3 shows the operational schematic of the SCDI diagnostic, and a thorough description of its operation is presented in [67]. In brief, it uses the Z-Beamlet Laser (ZBL) [68] to irradiate a manganese (Mn) foil target, which results in the laser ionization of the Mn target atoms to helium-like (He) charge states. After the rapid collisional ionization and radiative stabilization, the ions emit He_α K-shell X-rays. These so-called Mn-He_α (6.2-keV) X-rays are used to probe a shock-compressed sample on the Z-DMP load. The diffracted X-rays from the sample are reflected off the surface of a spherical crystal that has a radius of curvature R. The crucial aspect of this scheme is that the XRD sample is located on the Rowland circle that has a diameter R (e.g., the locus of focal points such that points on the circle are focused back onto the circle). As a result, the spherically bent crystal collects and focuses the diffracted X-rays into a detector housing with 1″ thick tungsten walls, where an image plate (IP) is used to store the XRD pattern. To achieve imaging with high spatial resolution ($\Delta x \approx 10$ μm), bent-crystal microscopes have nominally used various single-crystals such as quartz, mica, silicon, or germanium [69]. Alternatively, HOPG crystals have about 10–100× higher X-ray collection efficiency than these single-crystals [70] but have much lower spatial resolution due to their intrinsic mosaic spread. For the SCDI diagnostic, because of the intrinsically low signal levels of the Z-XRD measurement, a spherically bent HOPG crystal was selected to maximize the X-ray throughput.

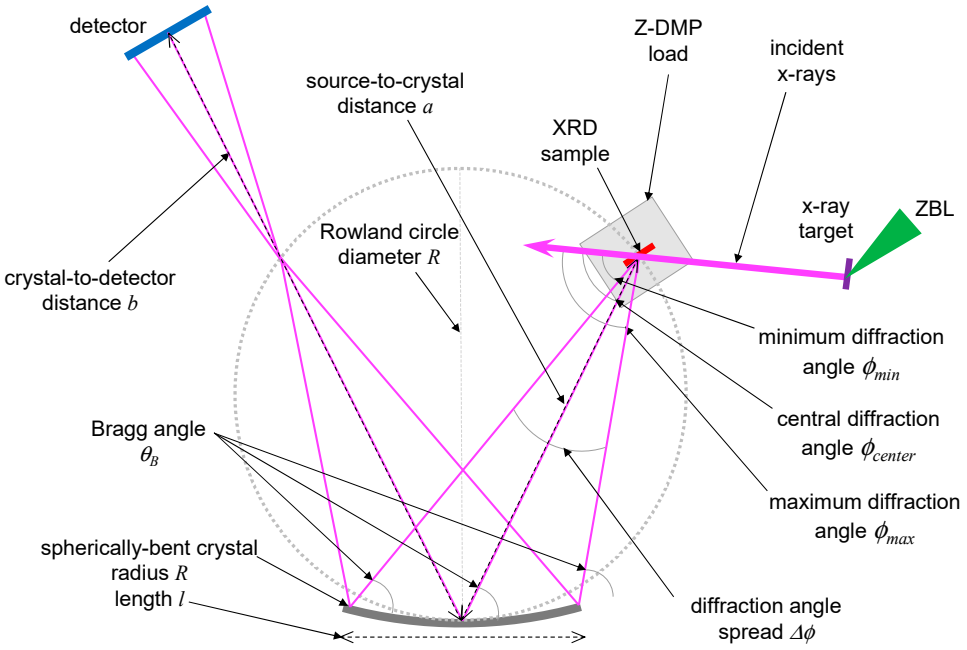

Figure 3. Operational schematic of SCDI diagnostic viewed in the meridional (horizontal) plane.

Figure 4 shows the hardware implementation of the SCDI diagnostic, which consists of two key components: (1) an imager ring and (2) a detector housing. The imager ring (~30-cm in diameter) surrounds the Z-DMP load, and all other SCDI parts are mounted directly on it. The ZBL X-ray target is mounted on the imager ring at a distance of 75 mm from the XRD sample. The spherically bent HOPG crystal (75-mm long by 30-mm tall) is affixed to a tip/tilt base that is mounted on the imager ring 135 mm from the XRD sample, and this source-to-crystal distance allows the collection of XRD patterns over a diffraction angle spread of ~30°. Due to debris generated by the load, the spherical crystal is single use. In addition, a cross-over aperture block (with a rectangular opening 3 mm wide × 15 mm tall) is mounted in front of the detector housing where the X-rays are intersected on the Rowland circle. Within the detector housing, an image plate (IP) detector is used to store the XRD data. The IP (75 mm wide by 35 mm tall) is contained inside a cassette that is retrieved after the Z-XRD experiment. Because it has several advantageous qualities, IP is used instead of other X-ray recording media. First, IP is a robust and reusable recording medium consisting of a highly X-ray sensitive phosphor crystals suspended in a plastic binder [71]. Second, IP has a dynamic range much larger than X-ray film and is capable of detecting X-rays with 1–100 keV photon energies [72,73]. Finally, IP is immune to the electromagnetic pulse interference of Z. Overall, the SCDI diagnostic is capable of measuring XRD patterns with angular resolution of ~1° and meridional spatial resolution of ~2 mm.

The SCDI diagnostic has successfully measured XRD patterns of shock-compressed samples on multiple Z-DMP experiments. However, several features of the SCDI diagnostic limit its viability to meet the long-term goals for XRD on Z. First, only X-rays at relatively low photon energies (4–10 keV) are viable with the SCDI scheme. For higher photon energies (>10 keV), higher reflection orders ($n > 4$) of the spherical HOPG crystal are required, but reflection intensity decreases with order. Second, the SCDI's sagittal focusing and the relatively poor imaging quality of HOPG crystals smear out any mesoscale features in the XRD patterns (e.g., grain size and preferred orientations). For these reasons, switching to a different X-ray detection technology is required to expand the capabilities of Z-XRD experiments.

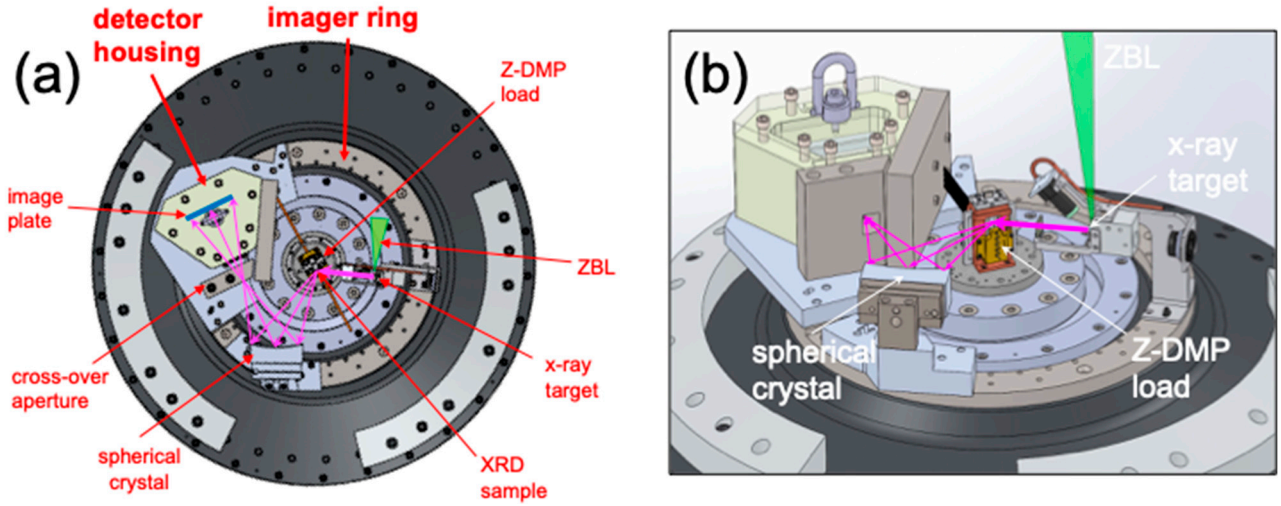

Figure 4. SCDI diagnostic on a Z-DMP experiment: (**a**) top view and (**b**) isometric view.

2.3.2. DIffraction SCintillator Optic (DISCO)

The overall purpose of the DIffraction SCintillator Optic (DISCO) imaging scheme is to detect an X-ray image generated inside a harsh, inaccessible environment with a high spatial (tens of μm) and temporal (~100 ns or shorter) resolution and relay the data to a protected digitizer in a safe location. Specifically, it requires the conversion of the diffracted X-rays to optical light, which is then transported away from the Z-DMP load and measured on a fast-gated camera (see Figure 5). The DISCO scheme incorporates time-gating to allow measurement only during the short time window of the laser-generated X-ray pulse in which XRD occurs. This, in turn, significantly reduces the unwanted X-ray background from the Z-DMP load.

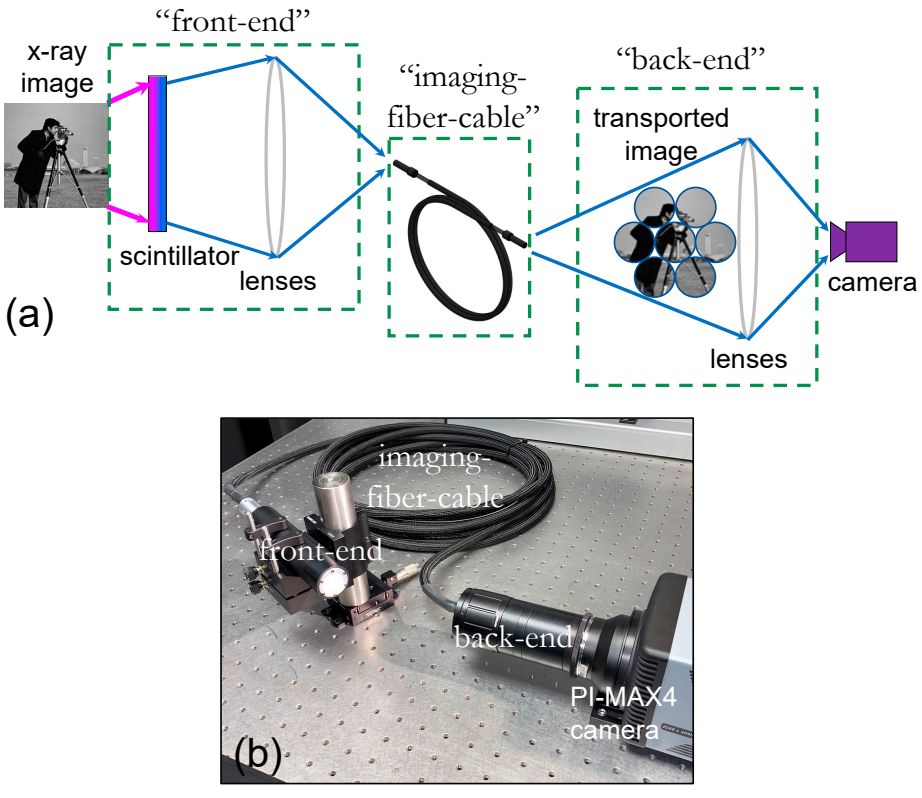

Figure 5. (**a**) Conceptual design of the DISCO scheme showing the front-end, imaging-fiber-cable, and back-end components and (**b**) hardware implementation.

Open beam optics [74] and fiber optic tapers [75,76] have previously been used separately to transport scintillator-converted X-rays-to-optical light to CCD detectors. A key feature of the DISCO scheme is that the scintillator is coupled to an optical imaging relay system that employs both open beam optics and an imaging fiber bundle. Furthermore, an assortment of scintillators could be used with the DISCO scheme, which have various decay times, emission wavelengths, and light yield (e.g., P43, P47, LSO, etc.). As shown in Figure 5a, the DISCO scheme consists of the following three components:

1. "front-end", passive X-ray-to-optical light converter (scintillator) and optical light collection optics (lenses);
2. "imaging-fiber-cable", passive imaging fiber bundle to transport the data out of the harsh environment;
3. "back-end", camera coupling optics (lenses) that can be attached to a commercial-off-the-shelf time-gated camera.

The hardware implementation of the DISCO diagnostic is shown in Figure 5b. The DISCO front-end consists of the scintillator (25 mm diameter) and 7 commercial-off-the-shelf lenses (30 mm diameter) mounted inside Thorlabs SM30 lens tubes. The lens package has the following parameters: achromatic, optimized for 380–550 nm; magnification of 0.261; input numerical aperture (NA) of 0.13; output NA of 0.447; total length of 154 mm; and a spatial resolution of 20 μm at the fiber and 50 μm at the scintillator. The DISCO imaging-fiber-cable consists of a hexagonal arrangement of 7 commercial-off-the-shelf 2 mm diameter imaging fibers (Asahi Multi-core POF MBL-2000-24); each is composed of 13,000 individual high-spatial-resolution PMMA (15 μm diameter) fibers, and together, they form a super-bundle (6 mm diameter). The imaging-fiber-cable has an NA of 0.485. The total length of the imaging-fiber-cable is 15 m, which corresponds to the approximate length needed to have the DISCO front-end fielded inside the Z-Center Section, exit a vacuum feed-through, and have the DISCO back-end fielded inside a screen box on the Z-Mezzanine. The DISCO back-end consists of 6 commercial-off-the-shelf and one custom lens, with the following parameters: achromatic, optimized for 380–550 nm; magnification of 3.3; object NA of 0.45 matched to the fiber; and a spatial resolution of 25 μm at the CCD and 7 μm at the fiber. The DISCO back-end was mounted to a PI-MAX4: 1024EMB-HBf Digital Intensified (emICCD) Camera System using a Thorlabs F-mount-to-SM2 adapter. The lens package fits within the aperture of a 1" zoom mount (Thorlabs SM2NR1) to adjust the image sharpness at the camera's focal plane array.

Figure 6 shows the hardware implementation of the DISCO diagnostic on a Z-DMP experiment. A similar imager ring is employed to allow all DISCO parts to be mounted directly on it. The ZBL X-ray target is mounted on the imager ring at Z's line-of-sight 245° location (LOS245) and at a distance of 75 mm from the XRD sample. The DISCO front-end is mounted on the imager ring so that the scintillator is 45 mm from the XRD sample, which enables about 30° of angular coverage for the XRD measurement. To align the DISCO front-end, a laser diode is initially fielded at the X-ray target location. The laser beam passes through an input collimator and is centered on the XRD sample. The laser beam is reflected off the XRD sample and onto the DISCO front-end, which has a nominal center diffraction angle 70° relative to the input X-rays. To cover various ranges of XRD angles, the DISCO front-end's center diffraction angle can be adjusted from 55° to 85°. One possible issue for the DISCO diagnostic would be darkening and/or fluorescence within the front-end and imaging-fiber-cable due to Z's X-ray background. Thus, a shielding tube and a nose cone were fabricated out of tungsten to contain the DISCO front-end. In addition, within the Z Center Section, part of the imaging-fiber-cable (~1-m in length) was fed through a steel interlocked armor shielding cable.

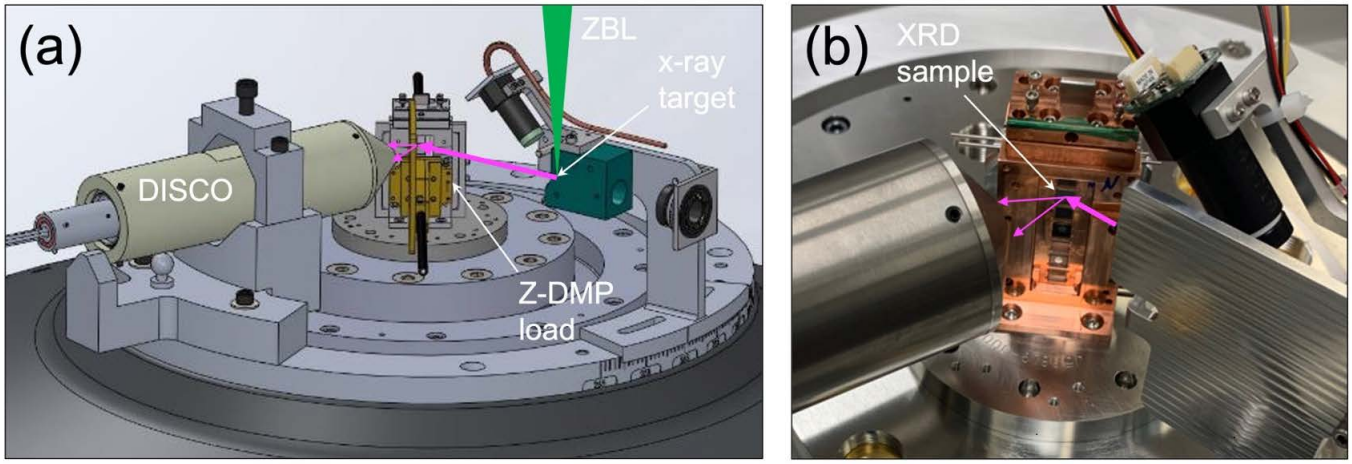

Figure 6. The DISCO diagnostic on a Z-DMP experiment: (**a**) isometric view rendering and (**b**) close-up photo.

3. Results

3.1. Ambient Calibrations

Carbon PG samples with mass densities of 2.1 g/cm^3 were obtained (Goodfellow), and their ambient XRD patterns were measured prior to the Z-DMP experiments. A carbon PG sample (5-mm wide by 5-mm tall by 1-mm thick) was placed near a Mn X-ray target that was irradiated by ZBL to generate 6.2 keV X-rays. At this X-ray photon energy, the carbon PG sample had a 1/e attenuation depth of 0.49 mm. A cylindrically curved IP was fielded to enable a wide angular range of XRD peaks to be simultaneously measured, as shown in Figure 7. The strong XRD peak at 34.9° and the weaker XRD peak at 73.6° were from the (002) and (004) hkl planes of the graphite-hexagonal structure (P6mc), respectively.

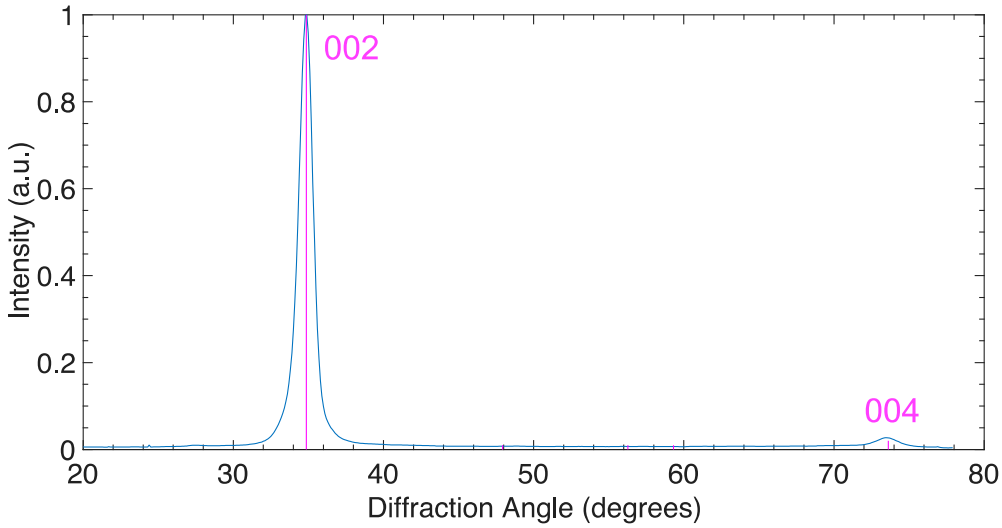

Figure 7. The measured XRD angular line profile of ambient carbon PG sample, where the vertical lines represent the predicted locations of the hexagonal structure's (002) and (004) hkl planes.

One long-term goal of Z-DMP experiments is to measure the XRD of high-Z material samples under dynamic compression, which is a challenge because the X-rays would not penetrate far beyond their free surfaces. As soon as the shock wave reaches the free surface, the high-pressure is immediately released so the XRD measurement would only be from the released state. Thus, an "X-ray window" is required to maintain a high-pressure state during dynamic compression while allowing for X-rays to probe the sample. Ambient beryllium has a hexagonal close-packed (hcp) structure (P63/mmc) and a mass density of

1.85 g/cm^3. For the 6.2 keV X-rays, beryllium has a substantial 1/e attenuation depth of 2.5 mm that enables high X-ray transmission during shock loading. Thus, ambient XRD data were also obtained from a beryllium window (1 mm thick), as shown in Figure 8. The ambient beryllium window's hcp structure had three prominent XRD peaks, at 60.9°, 68.1°, and 70.7° from the (100), (002), and (101) hkl planes, respectively. These XRD peaks are quite broad due to the long attenuation depth of the Be window, so the XRD data were obtained from its entire thickness.

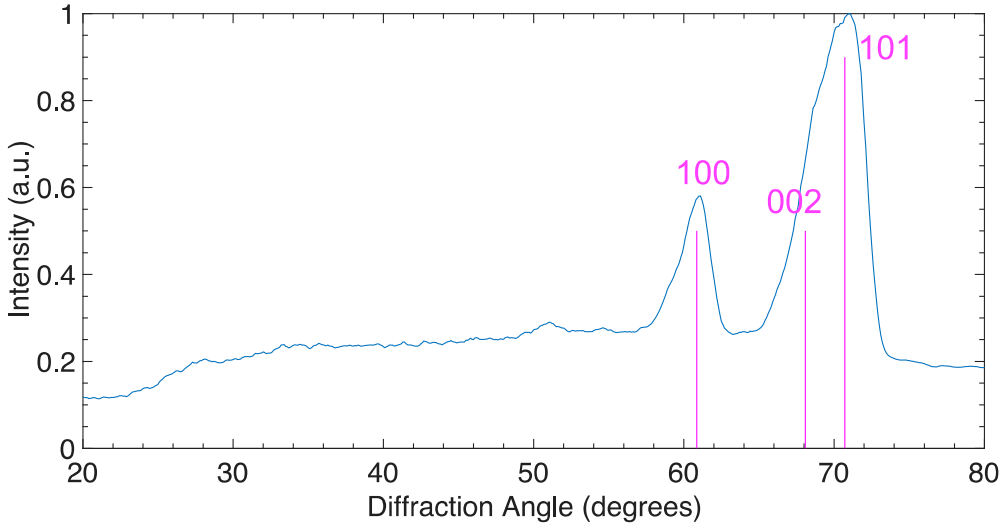

Figure 8. The measured XRD angular line profile of ambient beryllium window, where the vertical lines represent the predicted locations of the hcp structure's (100), (002), and (101) hkl planes.

3.2. Z-XRD Experiments

Three Z-XRD experiments, which have the designated Z shot numbers of Z3524, Z3710, and Z3717, have successfully returned XRD data on shocked carbon. For all the Z-XRD experiments, the flyer plates' velocities and impact times were measured by the VISAR diagnostic [63], and the timing of the incident X-rays was correlated to the arrival of the ZBL beam into the Z-Center Section. We employed the SCDI diagnostic on Z3524 and the DISCO diagnostic on Z3710 and Z3717. The experimental parameters of the Z-XRD experiments are listed in Table 1.

Table 1. Z-XRD experimental parameters.

Z Shot Number	Al Flyer Impact Velocity (km/s)	Impact Shock Pressure (GPa)	X-ray Window	Sample/X-ray Window Shock Pressure (GPa)	X-ray Diagnostic
Z3524	9.5	150	carbon	150	SCDI
Z3717	10.6	180	beryllium	150	DISCO
Z3710	15.0	320	carbon	320	DISCO

On Z3524, a 50-kV shaped pulse was used to launch an Al flyer to a peak velocity of 9.5 km/s that impacted a carbon PG sample (1.00 mm thick), as shown in Figure 9a. Using impedance-matching of the Al flyer (Sesame 3700 tabular EOS [77]), we inferred a shock pressure of 150 GPa in the carbon PG sample (see Figure 9b). The impedance-matching parameters are listed in Table 2.

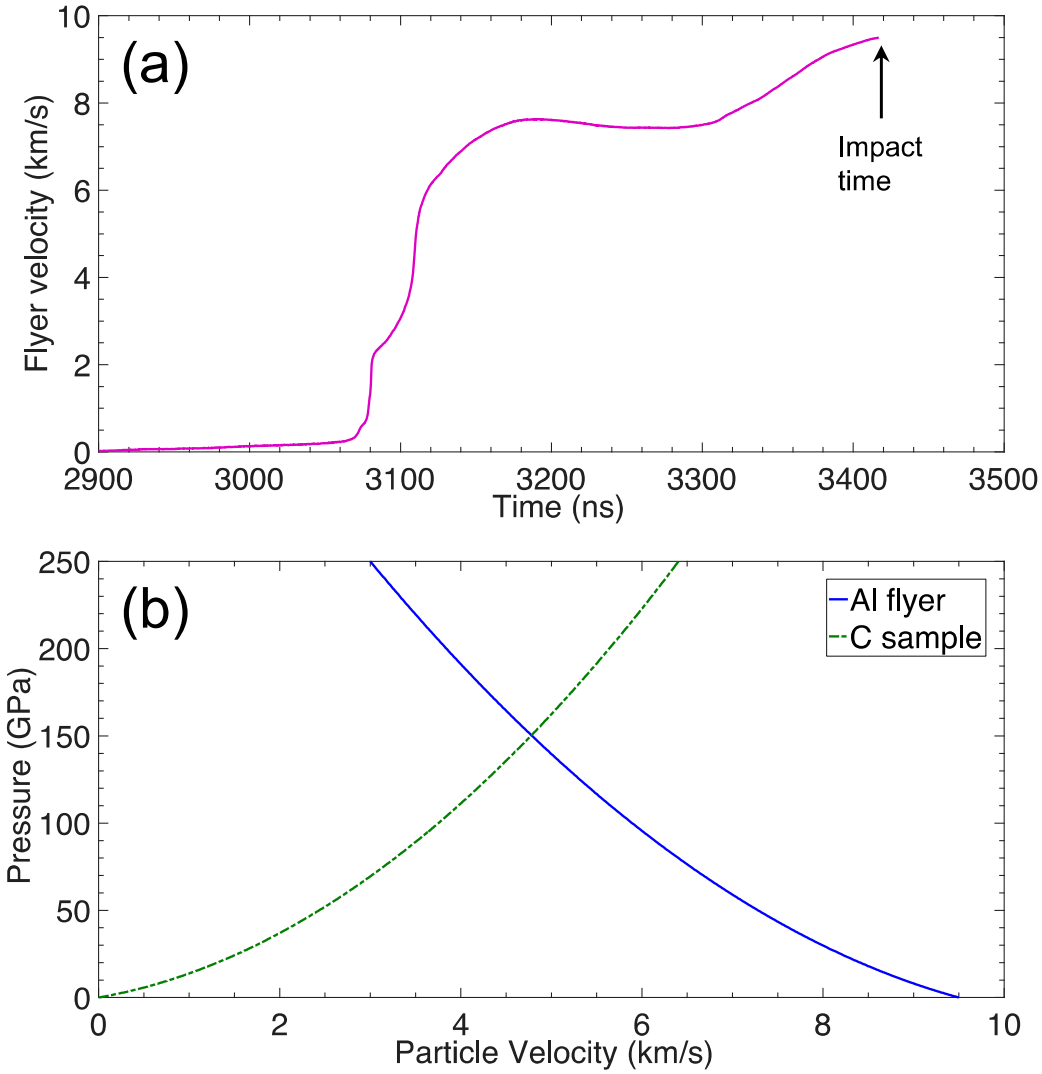

Figure 9. Z3524: (**a**) the Al flyer velocity history measured by the VISAR diagnostic up to the time of impact, and (**b**) the inferred shock pressure of the carbon sample using impedance-matching.

Table 2. Impedance-matching parameters.

Material	C (km/s)	S
Aluminum	5.288	1.376
Carbon graphite	4.260	2.170
Carbon diamond	18.33	2.070
Beryllium	7.998	1.124

The ZBL beam consisted of a pre-pulse (107 J, 0.5 ns) and a main pulse (2860 J, 3 ns). X-rays (6.2 keV) generated by the ZBL probed the carbon PG sample on the Z-DMP load's north panel. The ZBL was timed (20 ns after impact) to generate X-rays after the shock front had propagated 0.25 mm into the carbon PG sample. For Z3524, the carbon PG sample served as its own X-ray window during the shock loading, as shown in Figure 10a. The XRD signal measured by the SCDI diagnostic is shown in Figure 10b.

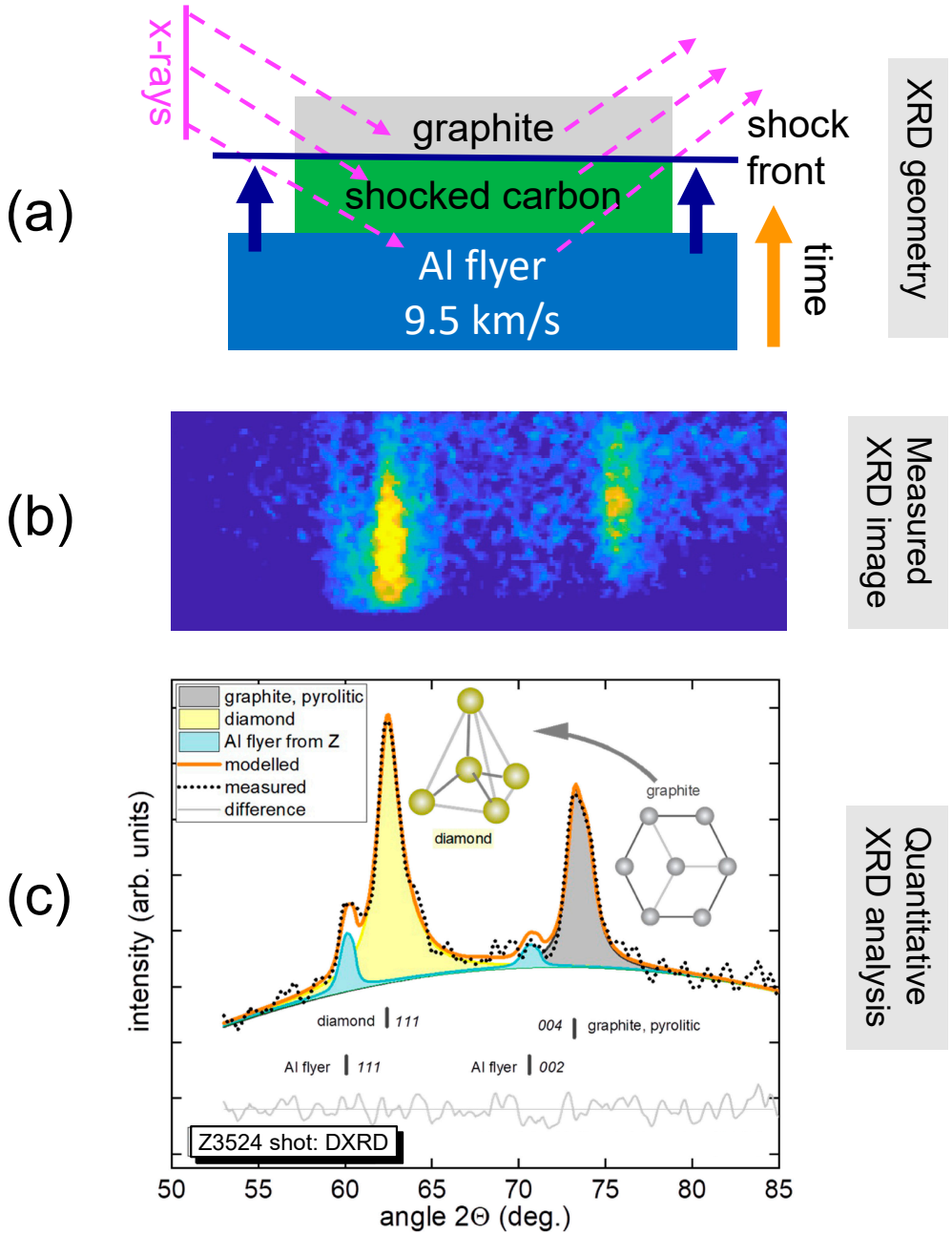

Figure 10. Z3524: the measured transformation of shock-compressed carbon graphite into diamond on a Z-DMP experiment using the SCDI diagnostic: (**a**) geometry of XRD measurement, (**b**) 2D X-ray image of XRD pattern, and (**c**) XRD angular line profile and corresponding Rietveld refinement.

Rietveld structural refinement [78] is a well-established method for the analysis of XRD data obtained in ambient, high-temperature, and high-pressure conditions, including in static compression with DAC technology. Recently, Rietveld refinement has been successfully applied to interpret XRD results from various shock compression experiments [79–81]. The Rietveld refinement of the SCDI data of Z shot number Z3524 showed clear X-ray diffraction signals from the cubic diamond phase (111) of the shocked carbon and the graphite hexagonal phase (004) from the ambient carbon, as shown in Figure 10c. In addition, weak XRD lines (111, 002) from the shocked Al flyer could be identified.

On Z3717, a 53-kV shaped pulse was used to launch an Al flyer to a peak velocity of 10.6 km/s (see Figure 11a) to impact a carbon PG sample (1.00 mm thick) backed by a beryllium window (0.60 mm thick). Using impedance-matching of the Al flyer, we inferred

an initial shock pressure of 180 GPa in the carbon sample (see Figure 11b). Then, as the shock wave propagated into the beryllium window, a rarefaction wave reflected from the sample-window boundary into the carbon and lowered its pressure state to 150 GPa.

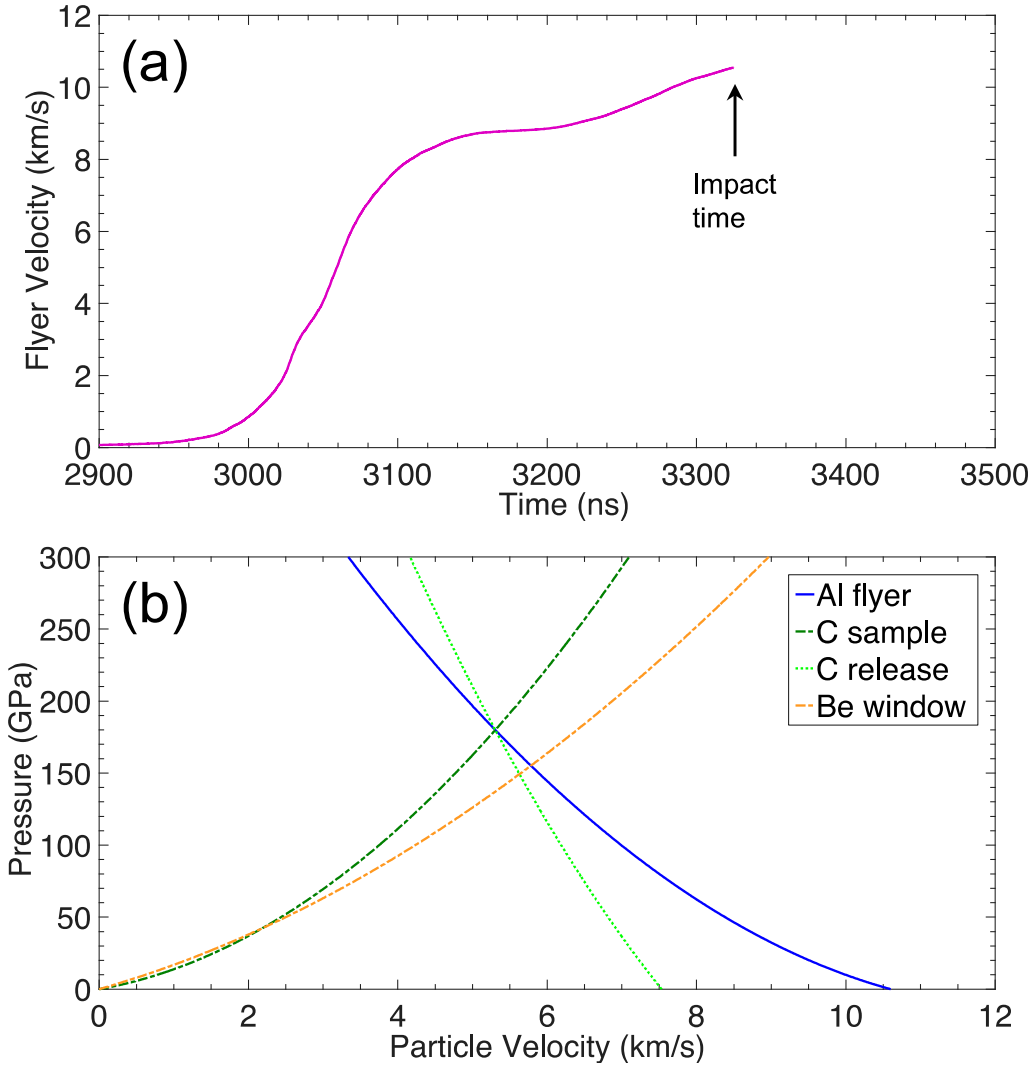

Figure 11. Z3717: (**a**) the Al flyer velocity history measured by the VISAR diagnostic up to the time of impact and (**b**) the inferred shock pressure of the carbon sample using impedance-matching.

The ZBL beam consisted of a pre-pulse (154 J, 0.5 ns) and a main pulse (2372 J, 3 ns) that was timed (99 ns after impact) to generate X-rays after the shock front had propagated completely through the carbon PG sample and about 0.2 mm into the beryllium window, as shown in Figure 12a. The DISCO front-end contained a P47 phosphor (100 ns decay), and the PI-MAX4 camera had a 150 ns gate window. Figure 12b shows the XRD recorded by the DISCO diagnostic, which contains multiple contributions from shocked, transformed, and unshocked materials, all present in the path of the X-ray beam. The XRD pattern analyzed with Rietveld refinement shows that the initial carbon PG material transformed into cubic diamond under shock compression (see Figure 12c). Also present are diffraction lines from the crystalline beryllium window and lines from shocked but untransformed graphite. The beryllium contribution consisted of both shocked and unshocked material as the shock wave had not transitioned through the entire Be window at the instant when the XRD measurement was taken.

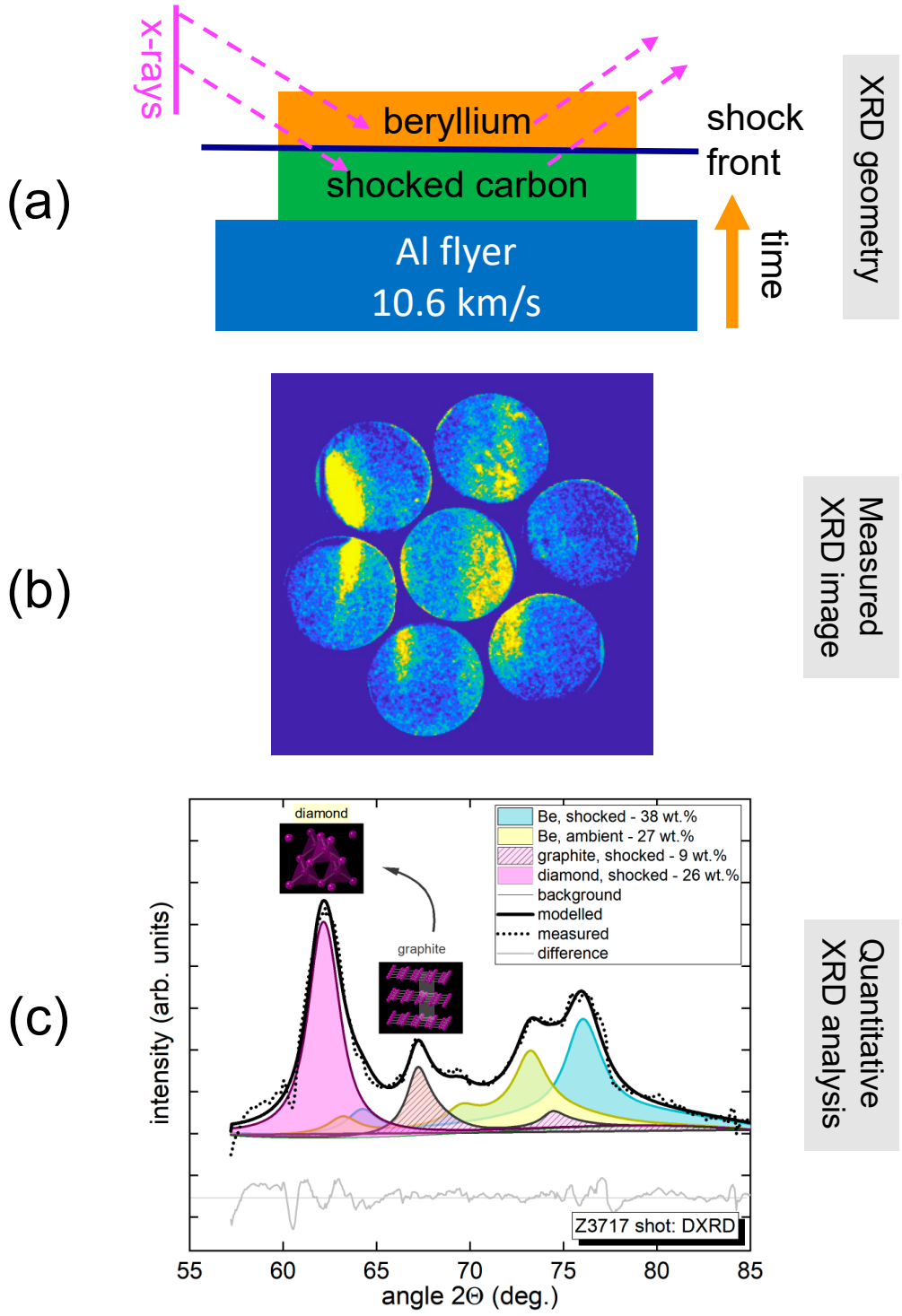

Figure 12. Z3717: the measured transformation of shock compressed carbon graphite into diamond on a Z-DMP experiment using the DISCO diagnostic: (**a**) geometry of XRD measurement, (**b**) 2D X-ray image of XRD pattern, and (**c**) XRD angular line profile and corresponding Rietveld refinement.

On Z3710, a 56-kV shaped pulse was used to launch an Al flyer to a peak velocity of 15.0 km/s (see Figure 13a) that impacted a carbon PG sample (0.98 mm thick). Using impedance-matching of the Al flyer, we inferred a shock pressure of 320 GPa in the carbon PG sample (see Figure 13b). For Z3710, the carbon PG sample also served as its own X-ray window during the shock loading.

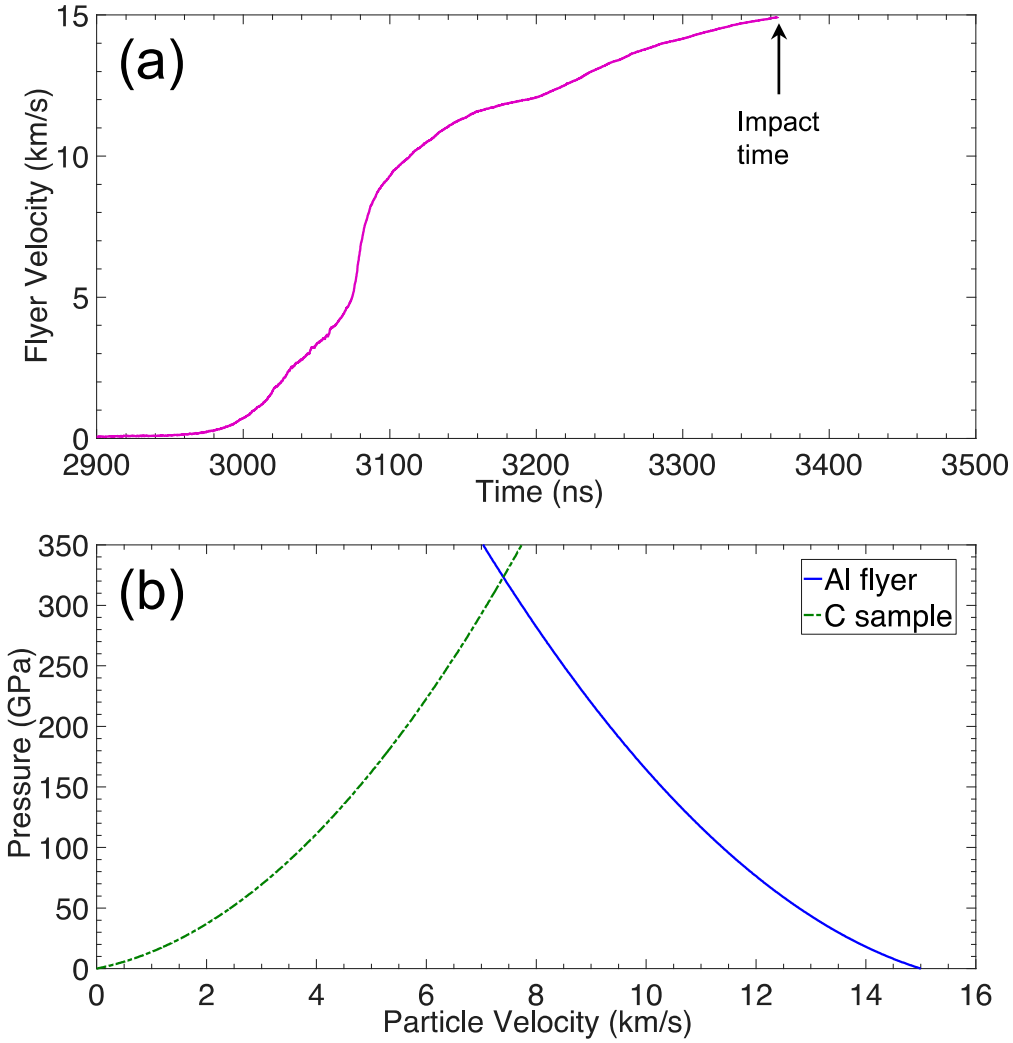

Figure 13. Z3710: (**a**) the Al flyer velocity history measured by the VISAR diagnostic up to the time of impact and (**b**) the inferred shock pressure of the carbon sample using impedance-matching.

The ZBL beam consisted of a pre-pulse (179 J, 0.5 ns) and a main pulse (2633 J, 3 ns) that was timed (45 ns after impact) to generate X-rays after the shock front had propagated through the 0.91 mm of the carbon PG sample, as shown in Figure 14a. The DISCO front-end contained a P47 phosphor (100 ns decay), and the PI-MAX4 camera had a 150 ns gate window. Due to the higher impact velocity, the carbon sample was shock-melted, and an overall broad X-ray feature was observed in the XRD pattern recorded by the DISCO diagnostic, as shown in Figure 14b. However, Rietveld refinement of the XRD pattern shows the remaining thin layer (0.07 mm thick) of ambient carbon PG in addition to the shocked-melted carbon (see Figure 14c).

In the Rietveld refinements, the refined parameters were a second-order Chebyshev background polynomial, as well as unit cell parameters of the respective crystal phases and peak profiles. Whereas the number of refined parameters was greater than the number of observed lines, the results of the refinements were used exclusively to confirm the presence of specific phases. The uncertainty in phase amounts was taken as three standard deviations from the refinement output (which tends to underestimate errors) and was between 5% (strong lines) and 10% (weak lines).

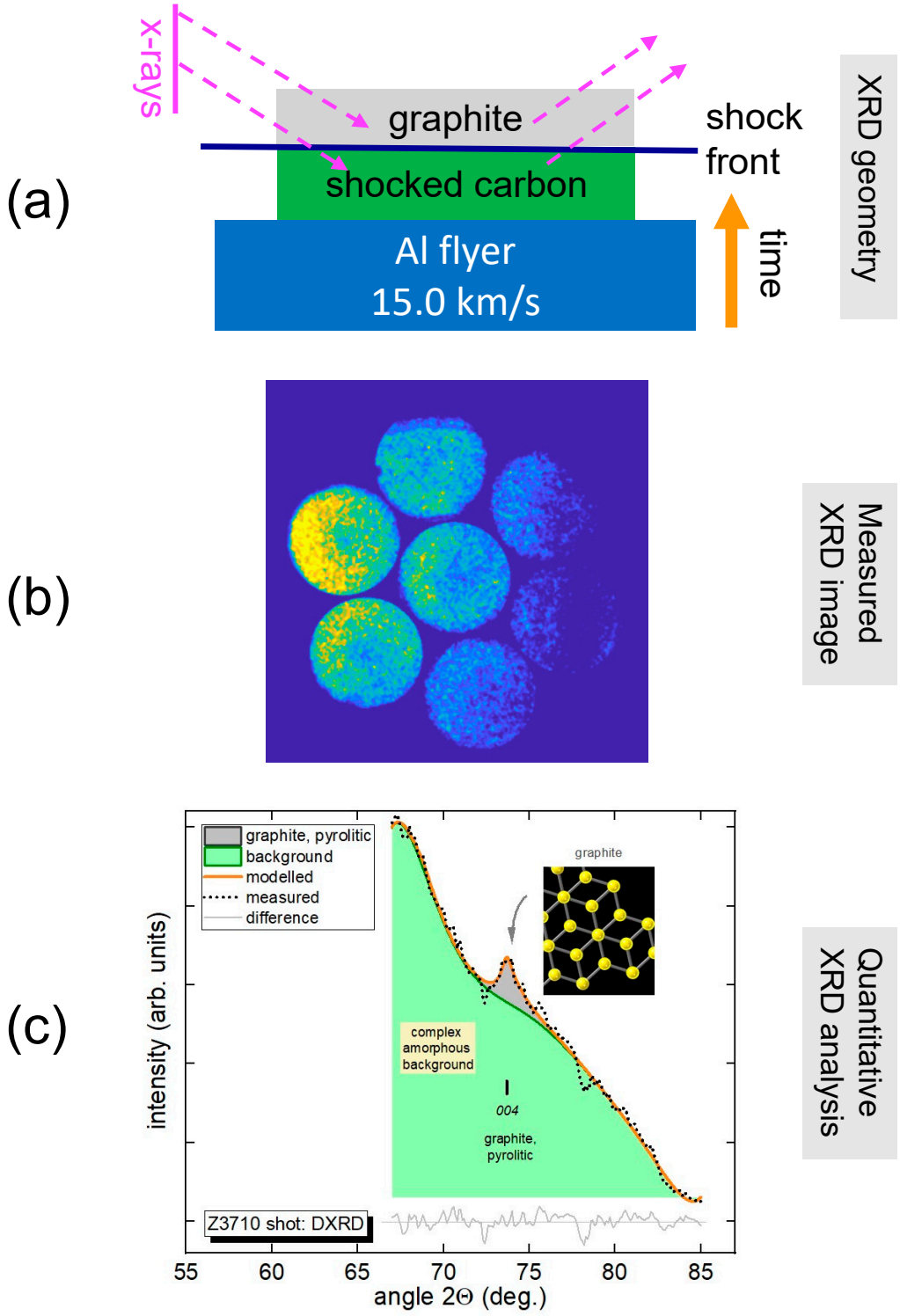

Figure 14. Z3710: the measured transformation of shock compressed carbon graphite into diamond on a Z-DMP experiment using the DISCO diagnostic: (**a**) geometry of XRD measurement, (**b**) 2D X-ray image of XRD pattern, and (**c**) XRD angular line profile and corresponding Rietveld refinement.

4. Discussion

The primary objective of this work was to develop new XRD diagnostic capabilities that have been sorely needed for DMP experiments on the Z Pulsed Power Facility. To implement and assess the XRD diagnostics on Z-DMP experiments, the shock compression of carbon was chosen. The secondary objective was to provide some useful shocked carbon

data for comparison with previous studies. The results from the Z-XRD experiments were compared with the laser-driven [45] and gas-gun plate impact [39–41] experiments. For all the Z-XRD experiments, carbon PG samples were dynamically compressed to pressures similar to the laser-driven experiments. The shock pressures were determined using the well-established method of impedance-matching that is used in gas-gun impact experiments and does not depend upon any simulations such as those used in the laser-driven experiments.

Shock-compressed carbon PG samples were observed to transform from the hexagonal graphite phase to the cubic diamond phase in two of the Z-XRD experiments (Z3524 and Z3717). On Z3524, the carbon PG sample served as its own X-ray window, so the impact pressure of 150 GPa was the in situ pressure of the shocked carbon. The Rietveld refinement identified all features within the XRD data of Z3524 to be from shocked cubic diamond, ambient hexagonal graphite, and shocked Al flyer. However, we observed no XRD features consistent with shocked hexagonal diamond. On Z3717, the impact pressure of the shocked carbon was 180 GPa, but then was lowered to 150 GPa at the beryllium X-ray window interface. This release resulted in a higher temperature at 150 GPa relative to Z3524. The Rietveld refinement identified all features within the XRD data of Z3717 to be from shocked cubic diamond, shocked hexagonal graphite, shocked beryllium, and ambient beryllium. Again, no XRD features could be identified to be from shocked hexagonal diamond. At the highest impact pressure of 320 GPa obtained on Z3710, the Rietveld refinement showed that almost all of the carbon PG sample had been shock-melted.

Overall, the presented Z-XRD experiments showed that the shock compression of typical hexagonal graphite (i.e., not HOPG) transformed to cubic diamond up to 150 GPa and melted above 320 GPa. In order to definitely investigate the claimed existence of hexagonal diamond, additional Z-XRD experiment would be required at the in-between shock pressures. Improvements to the Z-XRD diagnostics that are being pursued include using higher-photon-energy X-rays, increasing input X-ray flux, obtaining finer XRD angular resolution, and expanding XRD angular coverage. In addition, temperature measurements (e.g., pyrometry, radiometry) [82,83] would be needed to locate the shock states within the pressure–temperature phase space. However, experimental challenges remain on simultaneously measuring the temperature and XRD of dynamically compressed samples in Z-DMP experiments.

Author Contributions: Project lead, T.A.; conceptualization, T.A. and P.K.; experiment participants, T.A., P.K., C.B., K.F., N.P.B., P.G., H.H., M.G., M.M., S.P., E.S., A.S. and C.S.S.; data analysis, T.A. and P.K.; resources, J.L.P. and C.T.S.; writing—original draft preparation, T.A.; writing—review and editing, T.A., P.K., N.P.B. and C.T.S.; supervision, J.L.P. and C.T.S.; All authors have read and agreed to the published version of the manuscript.

Funding: Sandia National Laboratories is a multi-mission laboratory managed and operated by National Technology & Engineering Solutions of Sandia, LLC (NTESS), a wholly owned subsidiary of Honeywell International Inc., for the U.S. Department of Energy's National Nuclear Security Administration (DOE/NNSA) under contract DE-NA0003525.

Data Availability Statement: The data that support the findings of this study are available from the corresponding author upon reasonable request.

Acknowledgments: This written work is authored by an employee of NTESS. The employee, not NTESS, owns the right, title, and interest in and to the written work and is responsible for its contents. Any subjective views or opinions that might be expressed in the written work do not necessarily represent the views of the U.S. Government. The publisher acknowledges that the U.S. Government retains a non-exclusive, paid-up, irrevocable, worldwide license to publish or reproduce the published form of this written work or allow others to do so, for U.S. Government purposes. The DOE will provide public access to results of federally sponsored research in accordance with the DOE Public Access Plan.

Conflicts of Interest: The authors declare no conflict of interest.

References

1. Wang, X.; Scandolo, S.; Car, R. Carbon phase diagram from ab initio molecular dynamics. *Phys. Rev. Lett.* **2005**, *95*, 185701. [CrossRef]
2. Correa, A.A.; Bonev, S.A.; Galli, G. Carbon under extreme conditions: Phase boundaries and electronic properties from first-principles theory. *Proc. Nat. Acad. Sci. USA* **2006**, *103*, 1204–1208. [CrossRef]
3. Benedict, L.X.; Driver, K.P.; Hamel, S.; Militzer, B.; Qi, T.; Correa, A.A.; Saul, A.; Schwegler, E. Multiphase equation of state for carbon addressing high pressures and temperatures. *Phys. Rev. B* **2014**, *89*, 224109. [CrossRef]
4. Remington, B.A.; Drake, R.P.; Ryutov, D.D. Experimental astrophysics with high power lasers and Z pinches. *Rev. Mod. Phys.* **2006**, *78*, 755–807. [CrossRef]
5. Lindl, J.D.; Amendt, P.; Berger, R.L.; Glendinning, S.G.; Glenzer, S.H.; Haan, S.W.; Kauffman, R.L.; Landen, O.L.; Suter, L.J. The physics basis for ignition using indirect-drive targets on the National Ignition Facility. *Phys. Plasmas* **2003**, *11*, 339–491. [CrossRef]
6. Madhusudhan, N.; Lee, K.K.M.; Mousis, O. A possible carbon-rich interior in super-Earth 55 Cancri e. *Astrophys. J.* **2012**, *759*, L40. [CrossRef]
7. Segretain, L.; Chabrier, G.; Hernanz, M.; Garica-Berro, E.; Isern, J.; Mochkovitch, R. Cooling theory of crystallized white dwarfs. *Astrophys. J.* **1994**, *434*, 641–651. [CrossRef]
8. Metcalf, T.S.; Montgomery, M.H.; Kannan, A. Testing white dwarf crystallization theory with asteroseismology of the massive pulsating DA star BPM 37093. *Astrophys. J.* **2004**, *605*, L133–L136. [CrossRef]
9. Ross, M. The ice layer in Uranus and Neptune—Diamonds in the sky? *Nature* **1981**, *292*, 435–436. [CrossRef]
10. Hubbard, W.B. Interiors of gas giants. *Science* **1981**, *214*, 145–149. [CrossRef]
11. Benedetti, L.R.; Nguyen, J.H.; Caldwell, W.A.; Liu, H.; Kruger, M.; Jeanloz, R. Dissociation of CH_4 at high pressures and temperatures: Diamond formation in giant planet interiors? *Science* **1999**, *286*, 100–102. [CrossRef] [PubMed]
12. Abu-Shawareb, H.; Acree, R.; Adams, P.; Adams, J.; Addis, B.; Aden, R.; Adrian, P.; Afeyan, B.B.; Aggleton, M.; Aghaian, L.; et al. Lawson criterion for ignition exceeded in an inertial fusion experiment. *Phys. Rev. Lett.* **2022**, *129*, 075001. [CrossRef] [PubMed]
13. Zylstra, A.B.; Kritcher, A.L.; Hurricane, O.A.; Callahan, D.A.; Ralph, J.E.; Casey, D.T.; Pak, A.; Landen, O.L.; Bachmann, B.; Baker, K.L.; et al. Experimental achievement and signatures of ignition at the National Ignition Facility. *Phys. Rev. E* **2022**, *106*, 025202. [CrossRef] [PubMed]
14. Kritcher, A.L.; Zylstra, A.B.; Callahan, D.A.; Hurricane, O.A.; Weber, C.R.; Clark, D.S.; Young, C.V.; Ralph, J.E.; Casey, D.T.; Pak, A.; et al. Design of an inertial fusion experiment exceeding the Lawson criterion for ignition. *Phys. Rev. E* **2022**, *106*, 025201. [CrossRef]
15. Bernal, J.D. The structure of graphite. *Proc. R. Soc. A* **1924**, *106*, 749–773. [CrossRef]
16. Smith, W.H.; Leeds, D.H. Pyrolytic graphite. In *Modern Materials*; Gonser, B.W., Ed.; Academic Press, Inc.: New York, NY, USA, 1970; pp. 139–221. [CrossRef]
17. Guentert, O.J. X-ray study of pyrolytic graphites. *J. Chem. Phys.* **1962**, *19*, 884–891. [CrossRef]
18. Moore, A.W. Highly oriented pyrolytic graphite. In *Chemistry and Physics of Carbon*; Walker, P.L., Jr., Thrower, P.A., Eds.; Dekker: New York, NY, USA, 1973; Volume 11, pp. 69–187.
19. Fahy, S.; Louie, S.G. High-pressure structural and electronic properties of carbon. *Phys. Rev. B* **1987**, *36*, 3373–3385. [CrossRef]
20. Stachel, T.; Harris, J.W. Formation of diamond in the Earth's mantle. *J. Phys. Condens. Matter* **2009**, *21*, 364206. [CrossRef]
21. Field, J.E. The mechanical and strength properties of diamond. *Rep. Prog. Phys.* **2012**, *75*, 126505. [CrossRef]
22. Bundy, F.; Hall, T.; Strong, H.M.; Wentorf, R.H. Man-made diamonds. *Nature* **1955**, *176*, 51–55. [CrossRef]
23. Hazen, R.M. *The Diamond Makers*; Cambridge University Press: Cambridge, UK, 1999.
24. Hanneman, R.E.; Strong, H.M.; Bundy, F.F. Hexagonal diamonds in meteorites: Implications. *Science* **1967**, *155*, 995–997. [CrossRef]
25. Frondel, C.; Marvin, U.B. Lonsdaleite, a hexagonal polymorph of diamond. *Nature* **1967**, *214*, 587–589. [CrossRef]
26. Bundy, F.P.; Kasper, J.S. Hexagonal diamond—A new form of carbon. *J. Chem. Phys.* **1967**, *46*, 3437–3446. [CrossRef]
27. Nemeth, P.; Garvie, L.A.J.; Aoki, T.; Dubrovinskaia, N.; Dubrovinsky, L.; Buseck, P.R. Lonsdaleite is faulted and twinned cubic diamond and does not exist as a discrete material. *Nat. Commun.* **2014**, *5*, 5447. [CrossRef]
28. Salzmann, C.G.; Murray, B.J.; Shephard, J.J. Extent of stacking disorder in diamond. *Diam. Relat. Mater.* **2015**, *59*, 69–72. [CrossRef]
29. Bundy, F.P. Direct conversion of graphite to diamond in static pressure apparatus. *J. Chem. Phys.* **1963**, *38*, 631–643. [CrossRef]
30. Zhao, Y.X.; Spain, I.L. X-ray diffraction data for graphite to 20 GPa. *Phys. Rev. B* **1989**, *40*, 993–997. [CrossRef]
31. Yagi, T.; Utsumi, W.; Yamakata, M.A.; Kikegawa, T.; Shimomura, O. High-pressure in situ X-ray-diffraction study of the phase transformation from graphite to hexagonal diamond at room temperature. *Phys. Rev. B* **1992**, *46*, 6031–6039. [CrossRef]
32. DeCarli, P.S.; Jamieson, J.C. Formation of diamond by explosive shock. *Science* **1961**, *133*, 1821–1822. [CrossRef]
33. Erskine, D.J.; Nellis, W.J. Shock-induced martensitic phase transformation of oriented graphite to diamond. *Nature* **1991**, *349*, 317–319. [CrossRef]
34. Erskine, D.J.; Nellis, W.J. Shock-induced martensitic transformation of highly oriented graphite to diamond. *J. Appl. Phys.* **1992**, *71*, 4882–4886. [CrossRef]
35. Rygg, J.R.; Eggert, J.H.; Lazicki, A.E.; Coppari, F.; Hawreliak, J.A.; Hicks, D.G.; Smith, R.F.; Sorce, C.M.; Uphaus, T.M.; Yaakobi, B.; et al. Powder diffraction from solids in the terapascal regime. *Rev. Sci. Instrum.* **2012**, *83*, 113904. [CrossRef] [PubMed]
36. Rygg, J.R.; Smith, R.F.; Lazicki, A.E.; Braun, D.G.; Fratanduono, D.E.; Kraus, R.G.; McNaney, J.M.; Swift, D.C.; Wehrenberg, C.E.; Coppari, F.; et al. X-ray diffraction at the National Ignition Facility. *Rev. Sci. Instrum.* **2020**, *91*, 043902. [CrossRef]

37. Gleason, A.E.; Bolme, C.A.; Galtier, E.; Lee, H.J.; Granados, E.; Dolan, D.H.; Seagle, C.T.; Ao, T.; Ali, S.; Lazicki, A.; et al. Compression freezing kinetics of water to ice VII. *Phys. Rev. Lett.* **2017**, *119*, 025701. [CrossRef]
38. Turneaure, S.J.; Sinclair, N.; Gupta, Y.M. Real-time examination of atomistic mechanisms during shock-induced structural transformation in silicon. *Phys. Rev. Lett.* **2016**, *117*, 045502. [CrossRef]
39. Turneaure, S.J.; Sharma, S.M.; Volz, T.J.; Winey, J.M.; Gupta, Y.M. Transformation of shock-compressed graphite to hexagonal diamond in nanoseconds. *Sci. Adv.* **2017**, *3*, eaao3561. [CrossRef] [PubMed]
40. Volz, T.J.; Gupta, Y.M. Graphite to diamond transformation under shock compression: Role of orientational order. *J. Appl. Phys.* **2019**, *125*, 245902. [CrossRef]
41. Volz, T.J.; Turneaure, S.J.; Sharma, S.M.; Gupta, Y.M. Role of graphite crystal structure on the shock-induced formation of cubic and hexagonal diamond. *Phys. Rev. B* **2020**, *101*, 224109. [CrossRef]
42. Bradley, D.K.; Eggert, J.H.; Hicks, D.G.; Celliers, P.M.; Moon, S.J.; Cauble, R.C.; Collins, G.W. Shock compressing diamond to a conducting fluid. *Phys. Rev. Lett.* **2004**, *93*, 195506. [CrossRef]
43. Nagao, H.; Nakamura, K.G.; Kondo, K.; Ozaki, N.; Takamatsu, K.; Ono, T.; Shiota, T.; Ichinose, D.; Tanaka, K.A.; Wakabayashi, K.; et al. Hugoniot measurements of diamond under laser shock compression up to 2 TPa. *Phys. Plasmas* **2006**, *12*, 052705. [CrossRef]
44. Brygoo, S.; Henry, E.; Loubeyre, P.; Eggert, J.; Koenig, M.; Loupias, B.; Benuzzi-Mounaiz, A.; Rabec le Gloachec, M. Laser-shock compression of diamond and evidence of a negative-slope melting curve. *Nat. Mater.* **2007**, *6*, 274–277. [CrossRef]
45. Kraus, D.; Ravasio, A.; Gauthier, M.; Gericke, D.O.; Vorberger, J.; Frydrych, S.; Helfrich, J.; Fletcher, L.B.; Schaumann, G.; Nagler, B.; et al. Nanosecond formation of diamond and lonsdaleite by shock compression of graphite. *Nat. Commun.* **2016**, *7*, 10970. [CrossRef]
46. Knudson, M.D.; Desjarlais, M.P.; Dolan, D.H. Shock-wave exploration the high-pressure phases of carbon. *Sci. Rep.* **2008**, *322*, 1822–1825. [CrossRef]
47. Murri, M.; Smith, R.L.; McColl, K.; Hart, M.; Alvaro, M.; Jones, A.P.; Németh, P.; Salzmann, C.G.; Corà, F.; Domeneghetti, M.C.; et al. Quantifying hexagonal stacking in diamond. *Sci. Rep.* **2019**, *9*, 10334. [CrossRef]
48. Scandolo, S.; Bernasconi, M.; Chiarotti, G.L.; Focher, P.; Tosatti, E. Pressure-induced transformation path of graphite to diamond. *Phys. Rev. Lett.* **1995**, *74*, 4015–4018. [CrossRef]
49. Mundy, C.J.; Curioni, A.; Goldman, N.; Kuo, I.-F.W.; Reed, E.J.; Fried, L.E.; Ianuzzi, M. Ultrafast transformation of graphite to diamond: An ab initio study of graphite under shock compression. *J. Chem. Phys.* **2008**, *128*, 184701. [CrossRef] [PubMed]
50. Pineau, N. Molecular simulations of shock compressed graphite. *J. Phys. Chem. C* **2013**, *117*, 12778. [CrossRef]
51. Kroonblawd, M.P.; Goldman, N. Mechanochemcial formation of heterogenous diamond structures during rapid uniaxial compression in graphite. *Phys. Rev. B* **2018**, *97*, 184106. [CrossRef]
52. McQueen, R.G.; Marsh, S.P.; Taylor, J.W.; Fritz, J.N.; Carter, W.J. The equation of state of solids from shock wave studies. In *High-Velocity Impact Phenomena*; Kinslow, R., Ed.; Academic: New York, NY, USA, 1970; pp. 293–417. [CrossRef]
53. Duvall, G.E.; Graham, R.A. Phase transitions under shock-wave loading. *Rev. Mod. Phys.* **1977**, *49*, 523–579. [CrossRef]
54. Asay, J.R.; Mohsen, S. *High Pressure Shock Compression of Solids*; Springer: New York, NY, USA, 1993. [CrossRef]
55. Forbes, J.W. The history of the APS topical group on shock compression of condensed matter. In *Shock Compression of Condensed Matter—2001*; Furnish, M.D., Thadhani, N.N., Horie, Y., Eds.; American Institute of Physics: Melville, NY, USA, 2002; pp. 11–19. [CrossRef]
56. Forbes, J.W. *Shock Wave Compression of Condensed Matter: A Primer*; Springer: Berlin/Heidelberg, Germany, 2012. [CrossRef]
57. Band, W.; Duvall, G.E. Physical nature of shock propagation. *Am. J. Phys.* **1961**, *29*, 780–785. [CrossRef]
58. Mitchell, A.C.; Nellis, W.J. Shock compression of aluminum, copper and tantalum. *J. Appl. Phys.* **1981**, *52*, 3363–3374. [CrossRef]
59. Knudson, M.D.; Asay, J.R.; Deeney, C. Adiabatic release measurements in aluminum form 240- to 500-GPa states on the principal Hugoniot. *J. Appl. Phys.* **2005**, *97*, 073514. [CrossRef]
60. Celliers, P.M.; Collins, G.W.; Hicks, D.G.; Eggert, J.H. Systematic uncertainties in shock-wave impedance-match analysis and the high-pressure equation of state of Al. *J. Appl. Phys.* **2005**, *98*, 113529. [CrossRef]
61. Matzen, M.K.; Sweeney, M.A.; Adams, R.G.; Asay, J.R.; Bailey, J.E.; Bennett, G.R.; Bliss, D.E.; Bloomquist, D.D.; Brunner, T.A.; Campbell, R.B.; et al. Pulsed-power-driven high energy density physics and inertial confinement fusion research. *Phys. Plasmas* **2005**, *12*, 055503. [CrossRef]
62. Sinars, D.B.; Sweeney, M.A.; Alexander, C.S.; Ampleford, D.J.; Ao, T.; Apruzese, J.P.; Aragon, C.; Armstrong, D.J.; Austin, K.N.; Awe, T.J.; et al. Review of pulsed power-driven high energy density physics research on Z at Sandia. *Phys. Plasmas* **2020**, *27*, 070501. [CrossRef]
63. Barker, L.M.; Hollenbach, R.E. Laser interferometer for measuring high velocities of any reflecting surface. *J. Appl. Phys.* **1972**, *43*, 4669–4675. [CrossRef]
64. Sinars, D.B.; Bennett, G.R.; Wenger, D.F.; Cuneo, M.E.; Hanson, D.L.; Porter, J.L.; Adams, R.G.; Rambo, P.K.; Rovang, D.C.; Smith, I.C. Monochromatic X-ray imaging experiments on the Sandia National Laboratories Z facility (invited). *Rev. Sci. Instrum.* **2004**, *75*, 3672–3677. [CrossRef]
65. Bennett, G.R.; Sinars, D.B.; Wenger, D.F.; Cuneo, M.E.; Adams, R.G.; Barnard, W.J.; Beutler, D.E.; Burr, R.A.; Campbell, D.V.; Claus, L.D.; et al. High-brightness, high-spatial-resolution, 6.151 keV X-ray imaging of inertial confinement fusion capsule implosion and complex hydrodynamics experiments on Sandia's Z accelerator (invited). *Rev. Sci. Instrum.* **2006**, *77*, 10E322. [CrossRef]

66. Schollmeier, M.S.; Geissel, M.; Shores, J.E.; Smith, I.C.; Porter, J.L. Performance of bent-crystal X-ray microscopes for high energy density physics research. *Appl. Opt.* **2015**, *54*, 5147–5161. [CrossRef]
67. Ao, T.; Schollmeier, M.; Kalita, P.; Gard, P.D.; Smith, I.C.; Shores, J.E.; Speas, C.S.; Seagle, C.T. A spherical crystal diffraction imager for Sandia's Z Pulsed Power Facility. *Rev. Sci. Instrum.* **2020**, *91*, 043106. [CrossRef]
68. Rambo, P.; Schwarz, J.; Schollmeier, M.; Geissel, M.; Smith, I.; Kimmel, M.; Speas, C.; Shores, J.; Armstrong, D.; Bellum, J.; et al. Sandia's Z-Backlighter Laser Facility. *Proc. SPIE* **2016**, *10014*, 100140Z. [CrossRef]
69. Schollmeier, M.S.; Loisel, G.P. Systematic search for spherical crystal X-ray microscopes matching 1–25 keV spectral line sources. *Rev. Sci. Instrum.* **2015**, *87*, 123511. [CrossRef] [PubMed]
70. Ao, T.; Harding, E.C.; Bailey, J.E.; Loisel, G.; Patel, S.; Sinars, D.B.; Mix, L.P.; Wenger, D.F. Relative X-ray collection efficiency, spatial resolution, and spectral resolution of spherically-bent quartz, mica, germanium, and pyrolytic graphite crystals. *J. Quant. Spectrosc. Radiat. Transf.* **2014**, *144*, 92–107. [CrossRef]
71. Henke, B.L.; Gullikson, E.M.; Davis, J.C. X-Ray Interactions: Photoabsorption, Scattering, Transmission, and Reflection at E = 50–30,000 eV, Z = 1–92. *At. Data Nucl. Data Tables* **1993**, *54*, 181–342. [CrossRef]
72. Amemiya, T.; Miyahara, J. Imaging plate illuminates many fields. *Nature* **1998**, *336*, 89. [CrossRef] [PubMed]
73. Gales, S.G.; Bentley, C.D. Image plates as X-ray detectors in plasma physics experiments. *Rev. Sci. Instrum.* **2004**, *75*, 4001–4003. [CrossRef]
74. Madden, T.J.; McGuigan, W.; Molitsky, M.; Naday, I.; McArthur, A.; Westbrook, E.M. Lens-coupled CCD detector for X-ray crystallography. *IEEE Trans Nucl. Sci.* **2006**, *2*, 729–734. [CrossRef]
75. Naday, I.; Ross, S.; Westbrook, E.M.; Zental, G. Charge-coupled device/fiber optic taper array X-ray detector for protein crystallography. *Opt. Eng.* **1998**, *37*, 1235–1244. [CrossRef]
76. Gruner, S.M.; Tate, M.W.; Eikenberry, E.F. Charge-coupled device area X-ray detector. *Rev. Sci. Instrum.* **2002**, *73*, 2815–2842. [CrossRef]
77. Kerley, G.I. Theoretical equation of state for aluminum. *Int. J. Impact Eng.* **1987**, *5*, 441–449. [CrossRef]
78. Rietveld, H.M. A profile refinement method for nuclear and magnetic structures. *J. Appl. Cryst.* **1969**, *2*, 65–71. [CrossRef]
79. Gleason, A.E.; Bolme, C.A.; Lee, H.J.; Nagler, B.; Galtier, E.; Milathianaki, D.; Hawreliak, J.; Kraus, R.G.; Eggert, J.H.; Fratanduono, D.E.; et al. Ultrafast visualization of crystallization and grain growth in shock-compressed SiO_2. *Nat. Commun.* **2015**, *6*, 8191. [CrossRef] [PubMed]
80. Briggs, R.; Gorman, M.G.; Coleman, A.L.; McWilliams, R.S.; McBride, E.E.; McGonegle, D.; Wark, J.S.; Peacock, L.; Rothman, S.; Macleod, S.G.; et al. Ultrafast X-ray diffraction studies of the phase transitions and equation of state of scandium shock compressed to 82 GPa. *Phys. Rev. Lett.* **2017**, *118*, 025501. [CrossRef] [PubMed]
81. Kalita, P.; Specht, P.; Root, S.; Sinclair, N.; Schuman, A.; White, M.; Cornelius, A.L.; Smith, J.; Sinogeikin, S. Direct observations of a dynamically driven phase transition with in situ X-ray diffraction in a simple ionic crystal. *Phys. Rev. Lett.* **2017**, *119*, 255701. [CrossRef] [PubMed]
82. Eggert, J.H.; Hicks, D.G.; Celliers, P.M.; Bradley, D.K.; McWilliams, R.S.; Jeanloz, R.; Miller, J.E.; Boehly, T.R.; Collins, G.W. Melting temperature of diamond at ultrahigh pressure. *Nat. Phys.* **2009**, *6*, 40–43. [CrossRef]
83. Hartsfield, T.M.; Dolan, D.H. Establishing temperature from radiance of dynamically compresses metals. *J. Appl. Phys.* **2022**, *131*, 185901. [CrossRef]